Inorganic Chemistry

Article

pubs.acs.org/IC

Average and Local Structural Origins of the Optical Properties of the Nitride Phosphor $La_{3-x}Ce_xSi_6N_{11}$ ($0 < x \leq 3$)

Nathan C. George,[†,∥] Alexander Birkel,[†] Jakoah Brgoch,[†] Byung-Chul Hong,[‡] Alexander A. Mikhailovsky,[§] Katharine Page,[▽] Anna Llobet,[▽] and Ram Seshadri*[,†,⊥,#]

[†]Mitsubishi Chemical Center for Advanced Materials, University of California, Santa Barbara, California 93106, United States

[‡]Mitsubishi Chemical Corporation, Yokohama, Kanagawa 227-8502, Japan

[§]Department of Chemistry and Biochemistry, University of California, Santa Barbara, California 93106, United States

[▽]Lujan Neutron Scattering Center, Los Alamos National Laboratory, New Mexico 87545 United States

[∥]Department of Chemical Engineering, University of California, Santa Barbara, California 93106, United States

[⊥]Materials Department and Materials Research Laboratory, University of California, Santa Barbara, California 93106, United States

[#]Department of Chemistry and Biochemistry, University of California, Santa Barbara, California 93106, United States

Supporting Information

ABSTRACT: Structural intricacies of the orange-red nitride phosphor system $La_{3-x}Ce_xSi_6N_{11}$ ($0 < x \leq 3$) have been elucidated using a combination of state-of-the art tools, in order to understand the origins of the exceptional optical properties of this important solid-state lighting material. In addition, the optical properties of the end-member ($x = 3$) compound, $Ce_3Si_6N_{11}$, are described for the first time. A combination of synchrotron powder X-ray diffraction and neutron scattering is employed to establish site preferences and the rigid nature of the structure, which is characterized by a high Debye temperature. The high Debye temperature is also corroborated from ab initio electronic structure calculations. Solid-state ^{29}Si nuclear magnetic resonance, including paramagnetic shifts of ^{29}Si spectra, are employed in conjunction with low-temperature electron spin resonance studies to probes of the local environments of Ce ions. Detailed wavelength-, time-, and temperature-dependent luminescence properties of the solid solution are presented. Temperature-dependent quantum yield measurements demonstrate the remarkable thermal robustness of luminescence of $La_{2.82}Ce_{0.18}Si_6N_{11}$, which shows little sign of thermal quenching, even at temperatures as high as 500 K. This robustness is attributed to the highly rigid lattice. Luminescence decay measurements indicate very short decay times (close to 40 ns). The fast decay is suggested to prevent strong self-quenching of luminescence, allowing even the end-member compound $Ce_3Si_6N_{11}$ to display bright luminescence.

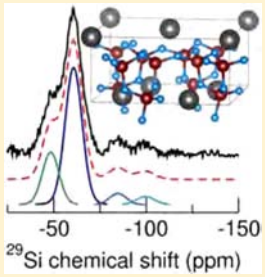

INTRODUCTION

Solid-state lighting (SSL) based on bright-blue InGaN light-emitting diodes (LEDs), combined with an efficient down-converting phosphor,[1−4] has attracted considerable attention in recent years, because of the many advantages that it offers. Solid-state white LEDs possess advantages of high efficiency, a mercury-free design, long lifetimes, color stability, and physically robust devices.[5,6] Since the use of yellow-emitting $Y_{3-x}Ce_xAl_5O_{12}$ (YAG:Ce) in solid-state white lighting devices in the mid-1990s,[7] many efforts have been exerted toward discovering new phosphors. Recently, researchers looking for new phosphors have tried materials containing many different anions, resulting in new host structures, such as oxysulfides and sulfides,[8] fluorosulfides,[9] oxyhalides,[10−12] oxynitrides,[13] and nitrides.[14−17] Nitrides are a promising candidate for solid-state lighting, because of their high quantum efficiencies[14] and good thermal quenching characteristics.[18] The smaller electronegativity of nitrogen, compared with oxygen, increases the covalency of nitride host lattices, compared with oxides. The increase in covalency results in the formation of highly rigid bonding networks. Although bond strength is defined rather arbitrarily in extended solids, using a proxy like the Debye temperature (Θ_D) to indicate a highly rigid lattice is a tractable substitute. A larger Θ_D value indicates that high-energy phonon modes are inaccessible, thereby decreasing the number of nonradiative relaxation pathways. Recent work has demonstrated Θ_D and the quantum efficiency are directly correlated, with a larger Θ_D value of the host compound usually yielding a high efficiency of the Ce^{3+}-substituted material.[19]

In addition, the center of gravity for the rare-earth 5*d* energy levels is shifted to lower values (this is termed the nephelauxetic effect) in compounds with the softer nitride anion, red-shifting emission.[20] It has also been suggested that the red-shift in emission of nitrides is strongly correlated with the anion polarizability,[21] or dielectric constant of the host lattice,[22,23] rather than simply the nephelauxetic effect. The higher formal charge of N, compared with that of O, also causes a larger crystal field splitting of the 5*d* levels of the activator ions in a nitride lattice, further red-shifting the emission.[24]

Received: September 12, 2013
Published: November 15, 2013

   dx.doi.org/10.1021/ic402318k | *Inorg. Chem.* 2013, 52, 13730−13741

Some examples of recently developed nitride phosphors include $(Ca,Sr,Ba)_2Si_5N_8:Eu^{2+}$,[14] $(Ca,Sr,Ba)YSi_4N_7:Eu^{2+}$,[25] the $Ca_3N_2-AlN-Si_3N_4:Eu^{2+}$ system,[26] $(Sr,Ba)SiN_2:Eu^{2+}/Ce^{3+}$,[27] $CaSiAlN_3:Ce^{3+}$,[28] and $LaSi_3N_5:Ce^{3+}$.[29] In phosphors such as $(Ca,Sr,Ba)_2Si_5N_8:Eu^{2+}$, Eu^{2+} can be fully substituted for the Ca/Sr/Ba site. Luminescence with 100% Ce^{3+} substitution has also been previously shown for CeF_3[30] and $CeMgAl_{11}O_{19}$,[31] which both emit in the UV range. In addition, blue luminescence of Ce^{4+} in Sr_2CeO_4 has been reported, with a long lifetime (65 μs) although with poor thermal robustness of the luminescence.[32,33] So far, full Ce^{3+} substitution has not been reported for a nitride phosphor compound, or a visible-light-emitting phosphor.

The host lattice structure of $La_{3-x}Ce_xSi_6N_{11}$ was first established in 1983 in the compound $Sm_3Si_6N_{11}$.[34] The structure, shown in Figure 1, is tetragonal and belongs to

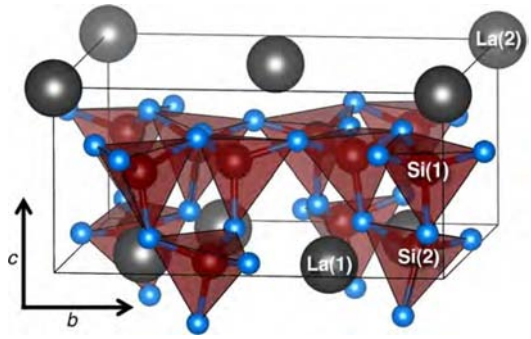

Figure 1. Crystal structure of $La_{3-x}Ce_xSi_6N_{11}$ looking down the *a*-axis. The atoms that compose the layers in the *a*–*b* plane have been labeled, with blue spheres representing N atoms.

space group *P*4*bm* (No. 100). It has two rare-earth (RE) sites and two Si sites; the RE sites have the same coordination number with slightly different geometries, but the Si sites are nearly identical in their nitrogen coordination. However, the Si sites have different connectivities to RE sites through their nitrogen bonds. After its discovery as $Sm_3Si_6N_{11}$, the compound was extended to many other RE ions in 1995, including $Ce_3Si_6N_{11}$, although the luminescent properties of this material were not studied at that time.[35] Schlieper et al. reported successful preparation of the $Ce_3Si_6N_{11}$ compound, noting that it was yellow, but studied the structure via X-ray diffraction (XRD) and the magnetic properties, not the optical properties.[36] $La_{3-x}Ce_xSi_6N_{11}$ was first studied as a phosphor material in 2009,[37,38] when it was shown that doping $La_{3-x}Ce_xSi_6N_{11}$ with small amounts of Ce^{3+} (on the order of 1 mol %) results in a compound with excitation in the blue region (~450 nm) that shows a bright, broad emission, which ranges from nearly 500 nm to 700 nm. The emission intensity of $La_{3-x}Ce_xSi_6N_{11}$ was shown to be very stable with temperature, which is an important characteristic of phosphors for use in practical devices. The emission intensity stability with temperature of $La_{3-x}Ce_xSi_6N_{11}$ is so extraordinary that it even exceeds the most temperature-stable oxide phosphors, namely $(Y,Gd)_3Al_5O_{12}:Ce^{3+}$.[37]

Although the $La_{3-x}Ce_xSi_6N_{11}$ crystal structure offers two La sites on which Ce can substitute, the emission spectra appear similar to other compounds with emission from only one site, such as YAG:Ce^{3+}. Previous studies on $La_{3-x}Ce_xSi_6N_{11}$ have not elucidated the distribution of Ce substitution on these two sites. Here, we use the complementary techniques of neutron diffraction, nuclear magnetic resonance (NMR), and electron spin resonance (ESR), to investigate the site occupancy of Ce on the two different crystallographic RE sites, and connect this to the optical properties. In addition, we use these techniques to explain the structural reasons for the remarkable thermal stability of emission intensity of $La_{3-x}Ce_xSi_6N_{11}$. Also, for the first time, we investigate the optical and structural properties of a fully Ce-substituted nitride phosphor: $Ce_3Si_6N_{11}$. Experimental studies are complemented by first-principles electronic structure calculations on the $La_3Si_6N_{11}$ host compound, establishing the large band gap (E_g) and high Debye temperature (Θ_D). Based on previous work,[19] we propose that both of these properties contribute to the high quantum efficiency and excellent robustness of luminescence of the nitride phosphor $La_{3-x}Ce_xSi_6N_{11}$.

MATERIALS AND METHODS

Electronic Structure Calculations. All calculations were carried out on the stoichiometric $La_3Si_6N_{11}$ using the Vienna ab initio simulation package (VASP),[39,40] using the projector augmented wave method (PAW) of Blöchl,[41] as adapted by Kresse and Joubert.[42] Initial relaxation of the atomic positions were performed to ensure that the compounds are in their electronic ground state. The elastic tensors were then determined from the stress–strain relationship of six finite distortions of the crystal[43] using displacements of ±0.015 Å. Exchange and correlation were described by the 1996 version of the Perdew–Burke–Ernzerhof generalized gradient approximation (PBE-GGA).[44] The energy cutoff of the plane wave basis set was 650 eV, and a 6 × 6 × 12 Monkhorst–Pack[45] *k*-mesh grid was used. The energy convergence criterion was set to 1×10^{-6} eV per formula unit, to ensure accurate electronic convergence. In addition to the elastic constants, the direct band gap for $La_3Si_6N_{11}$ was calculated using the more computationally intensive Heyd–Scuseria–Ernzerhof (HSE06) screened hybrid functional,[46,47] which is known to accurately reproduce experimentally measured band gaps in band insulators. These calculations employed a cutoff energy of 500 eV and a convergence criteria of 1×10^{-5} eV per formula unit.

Sample Preparation. $La_{3-x}Ce_xSi_6N_{11}$ was prepared from α-Si_3N_4 powder, LaN powder, CeO_2 powder, and CeN powder. CeN was prepared by nitridation of cerium metal under an ammonia (NH_3) flow. Two grams (2 g) of total starting reagents were ground in an alumina mortar and pestle in a glovebox, with pure nitrogen gas and oxygen and water vapor concentrations of <1 ppm. The ground powders were then loaded into a BN crucible. The crucible was set in a high-pressure furnace with carbon heaters and fired at 1580–2000 °C under 0.92 MPa nitrogen gas with a purity of >99.9995%. After the phosphor powders cooled to room temperature, they were ground into fine powders with an alumina mortar and pestle.

X-ray and Neutron Scattering. High-resolution synchrotron powder diffraction data were collected using the 11-BM beamline at the Advanced Photon Source (APS) at Argonne National Laboratory, at a temperature of 295 K and using an average wavelength of 0.4121540 Å. Additional details regarding the experimental setup can be found elsewhere.[48–50]

Neutron powder diffraction was performed on the HIPD and NPDF instruments at the Los Alamos Neutron Science Center at Los Alamos National Laboratory. Samples were placed in vanadium sample containers, and time-of-flight neutron data

dx.doi.org/10.1021/ic402318k | *Inorg. Chem.* 2013, 52, 13730–13741

was collected at 295 K on the HIPD instrument from eight detector banks at ±45°, ± 90°, ± 119° and ±148° 2Θ. For the NPDF measurements, samples were placed in vanadium cans, and time-of-flight neutron data was collected at 295 K from four detector banks, located at 14°, 40°, 90°, and 153° 2Θ. Crystal structures were refined using the EXPGUI[51] front end for the General Structure Analysis System (GSAS) refinement program.[52] Simultaneous refinements of the X-ray and neutron scattering data were completed by adjusting the profile shapes and backgrounds (10-term shifted-Chebyshev polynomial functions) during initial LeBail fits,[53] refining neutron absorption coefficients, instrument parameters, and the unit cell. These parameters were then kept static, and the neutron data only was used to refine the atomic positions, the atomic displacement parameters, and La/Ce occupancies. Occupancies and atomic displacement parameters are usually strongly correlated in Rietveld refinements, so these were refined in alternate cycles. Crystal structures were visualized using the software VESTA.[54] Debye temperatures for crystallographically distinct atoms ($\Theta_{D,i}$) were calculated from isotropic atomic displacement parameters using the high-temperature approximation:[55]

$$\Theta_{D,i} = \sqrt{\frac{3\hbar^2 T N_A}{A_i k_B U_{iso,i}}} \quad (1)$$

where i represents the atomic species La, Ce, Si, or N, and A_i is the atomic weight of the atom. The $U_{iso,i}$ values employed were the average of the individual atomic species in the unit cell, weighted by their Wyckoff multiplicities. The Debye temperature (Θ_D) for the material as a whole was then found by taking the weighted average of $\Theta_{D,i}$ from each atomic species, according to their stoichiometric coefficients in the formula $La_{3-x}Ce_xSi_6N_{11}$.

Solid-State ^{29}Si NMR and ESR. High-resolution solid-state NMR was used to investigate the local electronic environments of the $La_{3-x}Ce_xSi_6N_{11}$ materials. The single-pulse ^{29}Si NMR experiments were performed at 300 K on a Bruker AVANCE IPSO NMR spectrometer, with an 18.8 T narrow-bore superconducting magnet, operating at a frequency of 158.99 MHz for ^{29}Si nuclei, which are ∼5% naturally abundant. A Bruker 3.2 mm H-X-Y triple-resonance magic-angle spinning (MAS) probe head was used with zirconia rotors and Kel-F caps, with a MAS rate of 20 kHz. Radio-frequency (RF) pulse lengths and power levels were calibrated to achieve a 90° rotation of the net ^{29}Si magnetization (4 μs) and were calibrated with respect to the longitudinal spin−lattice relaxation time (T_1) to ensure the spectra were fully quantitative (recycle delay ranging from 300 to 0.25 s, depending on the Ce concentration). Because of the extremely fast relaxation of ^{29}Si in the $Ce_3Si_6N_{11}$ material, a Hahn-echo pulse sequence was used. This pulse sequence was used for all materials, along with ^{1}H decoupling. The pulse sequence consisted of a $\pi/2$ pulse, followed by a delay of 20 rotor periods, followed by a π pulse, and finally detection. The number of scans ranged from 128 (for samples with long relaxation times) to 16 000 (for $Ce_3Si_6N_{11}$). The MAS for the $Ce_3Si_6N_{11}$ material had to be initiated outside of the magnet, since the strong paramagnetism of the Ce^{3+} in the structure prevented the rotor from initializing spinning inside the magnetic field. ^{29}Si chemical shifts were referenced to tetramethylsilane (TMS) at −9.81 ppm.

^{29}Si spin−lattice relaxation-time behaviors of the $La_{3-x}Ce_xSi_6N_{11}$ samples were established using one-dimensional (1D) saturation−recovery MAS NMR spectra. 1D saturation-recovery ^{29}Si MAS NMR spectra were acquired for a range of times (τ) between 0.01 s and 1 s for the $Ce_3Si_6N_{11}$ material, and 0.01 and 300 s for the $La_{2.82}Ce_{0.18}Si_6N_{11}$ material, on the same spectrometer with the 18.8 T narrow-bore superconducting magnet used for the single-pulse ^{29}Si experiments. A RF pulse length of 4 μs was calibrated with the power level for a 90° rotation of the net magnetization of ^{29}Si nuclei, and a 400-pulse saturation train with 2 μs between saturation pulses with a 0.1 s recycle delay was used. Spectra were modeled using the simulation program dmfit.[56] The T_1 relaxation times of octahedral ^{29}Si nuclei were found by subsequently fitting the spectra from each delay time. The integrated intensity curves were then fitted with the curve fitting tool in MATLAB.

ESR spectra were collected on a Bruker X-band ESR spectrometer using an average microwave frequency of 9.486 GHz. Samples were placed in quartz tubes, and data were acquired at a temperature of 10 K.

Optical Measurements. Room-temperature photoluminescence (PL) spectra were obtained on a Perkin−Elmer Model LS55 spectrophotometer, scanning a wavelength range from 300 nm to 750 nm. The samples were thoroughly ground and subsequently mixed within a silicone resin. A small drop of the mixture was administered onto a small piece of glass and cured at 150 °C for 15 min. Photoluminescence quantum yield (PLQY) was measured with 457 nm excitation, using an argon laser and experimental protocol as described by Greenham et al.[57] Further details describing the employed setup, as well as the protocol to determine the temperature-dependence of the photoluminescence properties can be found elsewhere.[58,59] Diffuse reflectance UV/vis spectra were recorded in the wavelength range of 350−600 nm using a Shimadzu Model UV-3600 spectrometer equipped with an ISR-3100 integrating sphere. Samples were mixed with $BaSO_4$. The absorbance spectrum was obtained by applying the Kubelka−Munk[60] relation,

$$F(R) = \frac{(1-R)^2}{2R}$$

Luminescence lifetime measurements were performed using the time-correlated single photon counting (TCSPC) technique;[61] further details can be found in the Supporting Information.

RESULTS AND DISCUSSION

Evolution of Crystal Structure. The $La_{3-x}Ce_xSi_6N_{11}$ material can be prepared with values of x ranging from 0 to 3, which concurrently modulates the optical and structural properties. The symmetry of the compound does not change with composition. $La_{3-x}Ce_xSi_6N_{11}$ is tetragonal, crystallizing in the $P4bm$ space group (No. 100). The structure consists of layers of eight-coordinate LaN_8 polyhedra and SiN_4 tetrahedra, as shown in Figure 1. The La(1), La(2), and Si(2) sites are in almost the same plane parallel to the (001) plane, while the Si(1) sites are in their own separate plane parallel to the (001) plane. The Si(1)−N tetrahedra are fully corner-connected parallel to the (001) plane, and the Si(1)−N and Si(2)−N tetrahedra are corner-connected in the c-direction. This makes for a fully three-dimensional (3D) corner-connected SiN_4 tetrahedral network. Most N atoms bridge two Si tetrahedra,

the only N atom that bridges three Si tetrahedra is the N(3) site, which lies at the bottom of the Si(2) tetrahedra, as shown in Figure 1. The La(2) atoms share four three-sided faces of their polyhedra with the La(1) sites in the $a-b$ plane, and the La(1) sites share five corners of its polyhedra with other La(1) sites in the $a-b$ plane. As shown in Figure 2, the two La sites

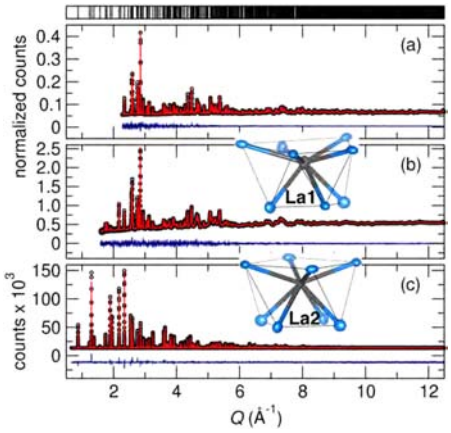

Figure 2. Simultaneous Rietveld refinement of $La_{2.82}Ce_{0.18}Si_6N_{11}$ scattering data at 295 K, showing (a) time-of-flight neutron data acquired on the NPDF instrument, (b) time-of-flight neutron data acquired on HIPD instrument, and (c) synchrotron X-ray data. A small amount (~1%) of $LaSi_3N_5$ impurity was included in the fit. The bars at the top of the figure show the expected reflection positions for the $La_3Si_6N_{11}$ phase. The inset polyhedra show the La(1) and La(2) sites with the 8 coordinating N atoms as ellipsoids representing 99% probability atomic displacement parameters. The polyhedra shown here are from the refinement of the $x = 0.18$ material.

have the same coordination number, but different polyhedral geometries. This manifests different site symmetries; La(1) has only a mirror plane (m), while La(2) has 4-fold rotational symmetry (4). One site, referred to herein as La(2)/Ce(2), has 4 N atoms above and 4 below in the $a-b$ plane in a square antiprism configuration, similar to other phosphor crystal structures such as $CaSc_2O_4$.[62] The other site, La(1)/Ce(1), has 5 N atoms above and 3 below in the $a-b$ plane, and an average La/Ce−N bond length (2.70 Å) that is ~3% larger than the La(2)/Ce(2) site (2.62 Å). The standard deviation of bond length of the La(1) site is also ~10−20 times larger than La(2). Although the site symmetries are different for the two La sites, the coordination numbers are identical and bond lengths quite similar. In this case, it appears the crystal field splitting of the Ce 5d levels is not significantly affected by the site symmetry, and Ce on either La site yields similar emission properties (see the optical properties below).

Rietveld refinement of synchrotron X-ray and neutron scattering from a single structural model enables one to probe the crystallographic parameters with great sensitivity. Synchrotron X-ray scattering is very sensitive to the unit-cell parameters of materials, and the extremely high flux from the radiation source enables unprecedented sensitivity for detecting impurities and subtleties in the unit cell symmetry. Neutron scattering, on the other hand, has form factors that do not vary with increasing Q, enabling a sensitive probe of atomic displacement parameters (ADPs). In addition, neutron scattering intensity does not follow the same periodic trend as in X-ray scattering, but instead nonsystematically varies with atomic number, enabling refinement of site occupancy of elements adjacent on the periodic table, such as La and Ce used in the materials here. Rietveld refinement of synchrotron X-ray and neutron scattering of the phosphor $La_{3-x}Ce_xSi_6N_{11}$, shown in Figure 2 and Table 1 for $La_{2.82}Ce_{0.18}Si_6N_{11}$, can therefore provide us with a sensitive probe to crystallographic parameters, impurities, ADPs, and site occupancy. For example, a small impurity (~1 mol %) of $LaSi_3N_5$ was observed in samples with low cerium content, while those with $x = 1.2$ and 2.1 had ~20 mol % of $LaSi_3N_5$ impurity. A full table of the crystallographic data from the refinements, including unit-cell parameters, site occupancies, and ADPs, is available in the Supporting Information. The unit-cell parameters of $La_{3-x}Ce_xSi_6N_{11}$ analyzed through Rietveld refinement of synchrotron X-ray scattering, displayed in Figure 3, show a linear decrease in unit-cell parameter a and decreasing cell volume with increasing cerium content, indicating materials in the $La_{3-x}Ce_xSi_6N_{11}$ solid solution obey the Végard law. This suggests the nominal amount of Ce is indeed incorporated into the lattice. The cell parameter c in Figure 3b essentially remains constant (within standard deviations) throughout the solid-solution series, showing that the contraction of the unit cell only occurs along the $a-b$ plane.

The nature of the site preference of Ce^{3+} was also investigated using Rietveld refinement of neutron data, and it

Table 1. Parameters from Rietveld Refinement of the $La_{2.82}Ce_{0.18}Si_6N_{11}$ Materials[a]

atom	Wyckoff symbol	x^b	y^b	z^b	F^b	$U_{iso}{}^{b,c}$
La(1) Ce(1)	4c	0.68080(4)	0.18080(4)	0.0147(1)	0.964(3) 0.036(3)	0.68(2)
La(2) Ce(2)	2a	0	0	0.9979(8)	0.873(4) 0.127(4)	0.34(2)
Si(1)	8d	0.20957(6)	0.07750(7)	0.5325(2)	1	0.14(3)
Si(2)	4c	0.11594(8)	0.61595(8)	0.0415(2)	1	0.26(3)
N(1)	8d	0.080348(3)	0.17834(3)	0.63787(2)	1	0.65(2)
N(2)	8d	0.23278(3)	0.07400(3)	0.17799(9)	1	0.54(1)
N(3)	4c	0.15310(3)	0.65310(3)	0.6944(1)	1	0.48(1)
N(4)	2b	0.5	0	0.0691(2)	1	0.78(2)

[a]The space group used in the refinement was $P4bm$, with unit-cell parameters of $a = 10.190734(4)$ and $c = 4.841258(3)$. [b]The estimated standard deviations for the last significant digit are given in parentheses. [c]The U_{iso} values [in (Å^2)] have been multiplied by 100.

dx.doi.org/10.1021/ic402318k | Inorg. Chem. 2013, 52, 13730−13741

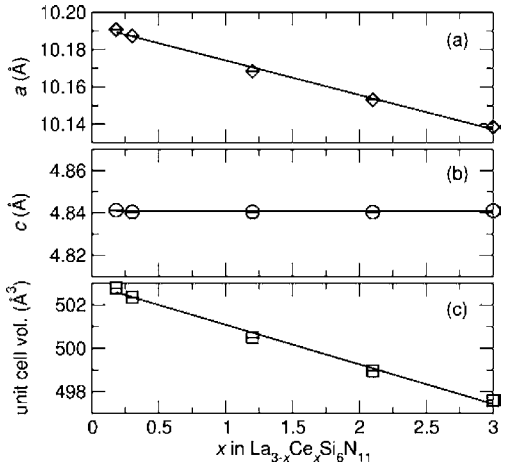

Figure 3. Unit-cell parameters of $La_{3-x}Ce_xSi_6N_{11}$ from Rietveld refinement of synchrotron powder X-ray diffraction (XRD) data acquired at 295 K, showing (a) cell parameter *a*, (b) cell parameter *c*, and (c) unit-cell volume *V*. Best-fit lines have been added to guide the eye.

shows that Ce^{3+} prefers to substitute on the La(2) site for low Ce concentrations. For a $La_{3-x}Ce_xSi_6N_{11}$ material with perfectly randomly distributed Ce atoms, the ratio of total Ce(1):Ce(2) would be 2:1 since the Wyckoff multiplicity of La(1) is twice that of La(2). Equivalently, the site fraction of Ce^{3+} on both the La(1) and La(2) sites would be equal. The results from Rietveld refinements in Figure 4a show that this ratio is found

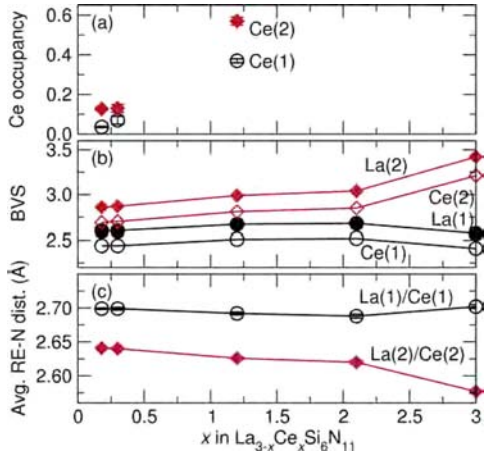

Figure 4. (a) Ce site occupancy of $La_{3-x}Ce_xSi_6N_{11}$ from Rietveld refinement of synchrotron X-ray and neutron scattering data acquired at 295 K, (b) bond-valence sums from Rietveld refinement, and (c) average La/Ce−N bond distance. Error bars represent estimated standard deviation from the refinements. Lines have been added to guide the eye.

to be 2:2.3 for the x = 0.18 material, 2:1.6 for the x = 0.3 material, and 2:1.5 for the x = 1.2 material. The refinements demonstrate that the amount of substituted Ce^{3+} is slightly larger than was intended in the preparation, especially for the x = 0.18 material. Preferential occupancy of the La(2) site by Ce^{3+} is not surprising, since the La(2) site has a slightly smaller average La−N distance compared to the La(1) site [2.70 Å for La(1) compared to 2.62 Å for La(2)]. The smaller ionic radii of 8-coordinate Ce^{3+} (1.143 Å) compared to 8-coordinate La (1.16 Å)[63] is consistent with Ce^{3+} favoring substitution on the smaller La site, La(2).

Calculation of the bond-valence sums (BVS)[64] for both Ce and La on sites 1 and 2, shown in Figure 4b, also support Ce favoring the La(2)/Ce(2) site. The bond lengths of the two La/Ce sites exhibited in Figure 4c demonstrate that the La(1)/Ce(1) site always has a larger bond length than the La(1)/Ce(1) site, regardless of Ce content. This results in a larger BVS for the La(2)/Ce(2) site that is much closer to the ideal value of 3 than for the La(1)/Ce(1) site as displayed in Figure 4(b). This trend only holds up to approximately x = 2, as demonstrated by the less than ideal BVS values for both La/Ce sites with x = 3. This indicates La and Ce may be more ideally bonded in the La(2)/Ce(2) site for lower Ce substitution levels. The BVS of the La(2)/Ce(2) site increases with Ce content, while the La(1)/Ce(1) site's BVS remains flat with increasing Ce substitution, a reflection of the variation in bond distances. The more ideal bonding environment of the La(2)/Ce(2) site is consistent with the apparent preference of Ce to substitute on the La(2)/Ce(2) site.

A comparison of the La(1) and La(2) U_{iso} values of $La_{2.82}Ce_{0.18}Si_6N_{11}$ shows the La(1) site has a U_{iso} of 0.0068(2), twice as large as that of La(2) [0.0034(2)], which is consistent with the longer La(1)−N_8 bond distances and greater variance in bond lengths compared to La(2)−N_8. The refinement results also show the U_{iso} of all atoms are on the order of 0.01 $Å^2$, indicating $La_{3-x}Ce_xSi_6N_{11}$ has a very rigid and well-ordered lattice. Θ_D, which is a rough estimate of the temperature at which the highest-energy phonon mode becomes populated, can be calculated from the isotropic displacement parameters.[55] Using the high-temperature approximation for calculation of Θ_D, we find Θ_D is at least 611 K for all materials investigated here. The Θ_D decreases slightly with increasing cerium content, going from 708 K (x = 0.18), to 645 K (x = 0.3), to 611 K (x = 1.2). The measured Debye temperature based on the U_{iso} values is in good agreement with the (ab initio) calculated Debye temperature of 660 K, described presently. The large Θ_D is one reason for the high quantum efficiency of the $La_{2.82}Ce_{0.18}Si_6N_{11}$ phosphor.

Electronic Band Structure of $La_3Si_6N_{11}$ Host. The experimental crystal structure of $La_{3-x}Ce_xSi_6N_{11}$ with x = 0.18 was used as a starting model for the crystal strucure of $La_3Si_6N_{11}$, which was relaxed using the PBE-GGA functional in first-principles DFT calculations. The relaxed structure of $La_3Si_6N_{11}$ converged to crystallographic parameters very close to those of $La_{3-x}Ce_xSi_6N_{11}$ with x = 0.18. The PBE-GGA relaxed structure was employed to determine the band structure displayed in Figure 5. Since PBE-GGA is known to underestimate the band gap of band insulators, the more computationally expensive HSE06 functional, known for attaining computed band gaps that are close to experimental values, was used to calculate the band structure at the special *k*-points in the Brillouin zone. The HSE06 calculations suggest that the host compound has a vertical band gap at the *Z* point of the Brillouin zone that is slightly larger than 4 eV. This is not a clear, direct band gap at Γ and potentially is advantageous in that band-edge absorption is not likely to be associated with a large extinction coefficient.

DFT calculations were also employed, using techniques described in ref 19 to calculate a Debye temperature of 660 K, for $La_3Si_6N_{11}$, which is close to what is observed experimentally.

Local Structure near Ce^{3+} and Site Preference from Solid-State ^{29}Si NMR. High-resolution solid-state MAS NMR

dx.doi.org/10.1021/ic402318k | *Inorg. Chem.* 2013, 52, 13730−13741

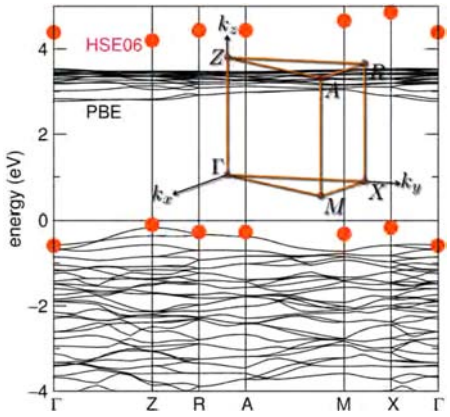

Figure 5. Calculated band structure of $La_3Si_6N_{11}$ from DFT calculations, carried out using the PBE-GGA functional (shown as connected lines) and, at special *k*-points, the HSE06 functional (shown as red circles). The inset is a depiction of the first Brillouin zone.

enables investigation of the local structure around the activator ions in phosphors. The paramagnetic dopant (activator) ion, Ce^{3+} in this case, can be used as a contrast reagent for NMR experiments, as has been seen before in pyrochlores,[65] stannates,[66] YAG:Tb^{3+},[67] and YAG:Ce^{3+}.[68] Here, the paramagnetic effects of the Ce^{3+} ion on surrounding ^{29}Si nuclei in $La_{3-x}Ce_xSi_6N_{11}$ are used to evaluate the local structure around Ce^{3+} and the site preference of its substitution. Since the relaxation time of an electron is very fast, interaction with a nearby paramagnetic ion causes the nuclear spins to relax quickly, a Hahn-echo pulse sequence was used to enable detection of quickly relaxing ^{29}Si species. The spectrum for x = 3 is the most simple to analyze, since there are only two ^{29}Si signals near −200 ppm and −38 ppm corresponding to the Si(1) and Si(2) sites, respectively, with the remaining peaks for x = 3 in Figures 6 and 7 being due to spinning sidebands. The ratio of ^{29}Si site 1 to ^{29}Si site 2 for the x = 3 material is 2.09:1—almost the expected value of 2:1. The discrepancy may be due to different relaxation times of the two sites and nonuniform loss of signal intensity during the Hahn-echo pulse sequence. The high degree of crystallinity in the samples, as seen in the X-ray and neutron scattering patterns, should manifest as narrow peaks in the NMR spectra, but the peaks are somewhat broad. This is due to the paramagnetic broadening induced by the large amount of Ce^{3+} in the lattice.[69]

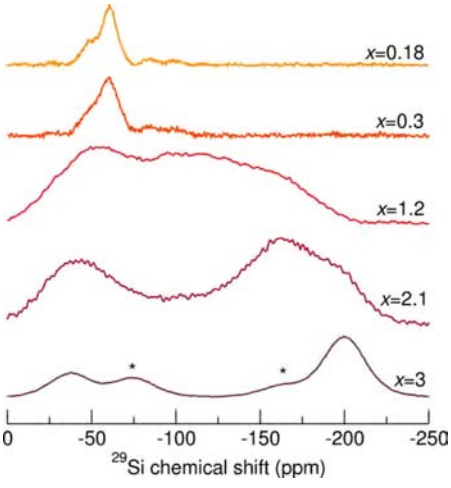

Figure 6. Solid-state Hahn-echo ^{29}Si MAS NMR spectra of $La_{3-x}Ce_xSi_6N_{11}$ acquired at 295 K, 20 kHz MAS, and 18.8 T, with x as indicated. The asterisks denote spinning sidebands. The spectra have been offset for clarity.

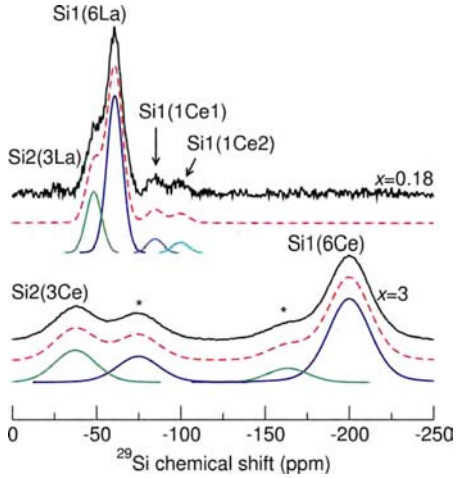

Figure 7. Solid-state Hahn-echo ^{29}Si MAS NMR spectra and multicomponent fits of $La_{3-x}Ce_xSi_6N_{11}$ acquired at 295 K, 20 kHz MAS, and 18.8 T, with x as indicated. Asterisks denote spinning sidebands. Peaks are labeled with the corresponding Si site in Table 2, with some of the nearest lanthanide atoms indicated in parentheses. The spectra and fits have been offset for clarity.

As the amount of La is increased and the amount of Ce decreased, the Si(1) signal moves to a higher frequency at approximately −61 ppm, and the Si(2) signal moves to −49 ppm for the x = 0.18 material. The ^{29}Si spectra of $La_{2.7}Ce_{0.3}Si_6N_{11}$ and $La_{2.82}Ce_{0.18}Si_6N_{11}$ in Figure 6 are both very similar, with two main ^{29}Si signals at approximately −61 ppm and −49 ppm, corresponding to the crystallographic Si sites Si(1) and Si(2), respectively. The other small peaks near −85 ppm and −100 ppm are ^{29}Si nuclei near substituted Ce^{3+} in the materials. These signals are displaced to lower frequencies (more negative ppm values), which is toward the Si(1) peak for the x = 3 material. Since the Si(2) signal is in the opposite direction (higher frequency or less negative ppm values), the displaced peaks near −85 ppm and −100 ppm are associated with the $^{29}Si(1)$ site nuclei. Taking this into account, the ratio of the $^{29}Si(1)$ site to the $^{29}Si(2)$ site for the x = 0.18 material is 3:1, which is much larger than the nominal 2:1 ratio observed from the Wyckoff multiplicities. An overestimation of the Si(1) population is consistent with what was seen in the NMR spectra for the x = 3 material. This may be related to nonuniform signal loss from different ^{29}Si sites, because of the Hahn-echo pulse sequence. Paramagnetic ions such as Ce^{3+} are known to displace the signal of NMR-active nuclei,[65] with the displacement dependent on the orientation of the nearby ^{29}Si nuclei, with regard to a Ce^{3+} atom in the lattice. To predict the directions and magnitudes of the paramagnetic displacements, one requires crystal-field splitting tensors of Ce^{3+}. However, these have not been measured or calculated for Ce^{3+} in $La_{3-x}Ce_xSi_6N_{11}$, so, as a first approximation, a cylindrical symmetry of the crystal-field splitting tensors can be assumed. Since the mirror-plane and 4-fold symmetries of the two La/Ce sites are parallel to the *c*-axis in the $La_{3-x}Ce_xSi_6N_{11}$ unit cell, we assume the principal magnetic axis of symmetry for the Ce atoms in both sites lies along the *c*-direction. With this assumption, the angular factors that contribute to calculation of

dx.doi.org/10.1021/ic402318k | Inorg. Chem. 2013, 52, 13730−13741

the paramagnetic displacements[70] would be equivalent for the eight Si atoms surrounding a Ce(1) site, and would be equivalent for the eight Si atoms nearest a Ce(2) site. Assuming the crystal-field splitting tensor values are nearly the same for Ce on the two sites, the only other parameter that will effect the paramagnetic displacement is the internuclear Ce^{3+}−Si distance. The magnitude of the paramagnetic displacement is related to the internuclear Ce^{3+}−^{29}Si distance as $1/r^3$. Since the Si(1) distance to La/Ce(1) is 3.61 Å and to La/Ce(2) is 3.32 Å, the induced shift on Si(1) from a Ce(2) site is expected to be of greater magnitude than that from a Ce(1) site. The peaks in the fit in Figure 7 were assigned based on this inference, and the ratio of the two Ce sites can be analyzed to understand the site preference of Ce. Combinatorial analysis with a random distribution of Ce in the lattice says the ratio of Ce site 1 to Ce site 2 should be 2:1, since there are twice as many Ce(1) sites in the structure. The ratio from the NMR spectra here gives a ratio of 2:1.6 for the x = 0.18 material and 2:1.7 for the x = 0.3 material, showing Ce has a strong preference for site 2. This agrees with the Rietveld and BVS analysis for x = 0.3 (Ce(1):Ce(2) of 2:1.6), but is much less than the 2:2.3 ratio obtained for x = 0.18. Back-calculating the amount of substituted Ce from integration of the NMR spectra gives a result of 1.6% for the 6% Ce (x = 0.18) doped material, and 2.4% for the 10% Ce (x = 0.3) doped material. The very low underestimate of total Ce substitution may be due to substantial loss of signal intensity from T_2 relaxation of ^{29}Si nuclei near substituted Ce^{3+} ions.

Fits of the x = 1.2 and x = 2.1 materials were infeasible, since a combinatorial analysis predicts 15 peaks from distinct ^{29}Si sites with different amounts of Ce ions nearby. These peaks would also have spinning sidebands that would convolve with the fit, adding another 30 Gaussian peaks to the fit. Although we can see the gradual trend of the Si(1) signal moving to lower frequency, direct analysis of the Ce(2)/Ce(1) ratio from these spectra is challenging.

From the x = 0.18 spectra in Figure 6, the displacement of the Si(1) chemical shift from a nearby Ce(1) is found to be approximately −24 ppm, and −38 ppm from a nearby Ce(2) ion. These shifts are consistent with the −200 ppm position of the Si(1) in the x = 3 material, since there are 2 Ce(2) ions and 4 Ce(1) ions near each ^{29}Si(1) atom, for a total shift of −172 ppm, which would yield a signal at approximately −233 ppm. However, because each Ce near a ^{29}Si atom is a distinct distance away, this generalized approach fails to perfectly predict the total displacement amount of the ^{29}Si(1) signal, but appears to be a good approximation. The signal associated with the Si(2) site is not displaced as far as the Si(1) site as Ce substitution increases from x = 0.18 to x = 3, and is shifted toward higher frequency with addition of Ce in the lattice. This is because the Si(2) site is in the same plane as the three nearest Ce sites, which causes the anisotropic magnetic susceptibility of Ce to interact more weakly with the Si(2) site than the Si(1) site. In terms of the equation for the dipolar pseudo-contact shift,[65,70] this means the angle between the principal magnetic axis of symmetry of Ce^{3+} and the Ce−Si(2) internuclear distance is ∼55° or ∼125°, which makes the paramagnetic NMR signal displacement nearly zero. In other words, the principal magnetic axis of symmetry of Ce^{3+} on site 2 is ∼55° or ∼125° away from the *ab*-plane in the $La_{3-x}Ce_xSi_6N_{11}$ unit cell.

The fwhm of the ^{29}Si peaks also increases with increased cerium content, as seen in Table 2. However, the fwhm of the paramagnetically displaced peaks is not significantly greater than the bulk peaks in both the x = 0.18 and x = 0.3 Ce-doped samples, indicating uniform environments and a high amount of crystallinity around the substituted Ce^{3+} ions. This likely relates to the high quantum efficiencies and resistance to thermal quenching seen in $La_{3-x}Ce_xSi_6N_{11}$, as well as the high Θ_D calculated from the U_{iso} values obtained from Rietveld analyses.

Table 2. Populations, Chemical Shifts, Full Width at Half Maximum (fwhm), and Relaxation Times (T_1) for ^{29}Si sites in $La_{3-x}Ce_xSi_6N_{11}$, with the Different Compositions Labeled

Si site[a]	population (%)	chemical shift (ppm)	fwhm	T_1
		$La_{2.82}Ce_{0.18}Si_6N_{11}$		
1(6La)	65.7	−61.2	10.9	20.0
2(3La)	24.6	−48.8	10.6	18.3
1(1Ce(1))	5.4	−85.1	10.8	0.921
2(1Ce(2))	4.3	−99.5	11.8	0.997
		$La_{2.7}Ce_{0.3}Si_6N_{11}$		
1(6La)	67.6	−60.5	14.6	19.84
2(3La)	21.8	−47.1	11.4	16.76
1(1Ce(1))	11.2	−84.5	11.7	0.8345
2(1Ce(2))	8.5	−99.9	12.8	0.9651
		$Ce_3Si_6N_{11}$		
1(6Ce)	67.6	−200.4	29.8	0.0572
2(3Ce)	32.4	−37.7	29.0	0.105

[a]Some of the nearest lanthanide ions are given in parantheses.

To further investigate the properties of the materials, saturation−recovery experiments were performed. These experiments saturate the magnetization of NMR-active nuclei, then after a delay time perform a normal NMR experiment. This allows measurement of the T_1 relaxation times of the different components in the spectra (by fitting the integrated areas as a function of time to an exponential function), and can separate the fast-relaxing components from the slow relaxing components. Figure 8, which shows a set of saturation−recovery experiments performed on $Ce_3Si_6N_{11}$, shows that the two Si sites have very fast relaxation times (∼0.05 and 0.1 s for the Si(1) and Si(2) sites in the structure, respectively). The fast T_1 values are due to the large amount of Ce^{3+} in the structure, which has an unpaired electron that interacts with the ^{29}Si nuclear spins and causes much shorter relaxation times. Figures 9a and 9b show that the $La_{2.82}Ce_{0.18}Si_6N_{11}$ bulk ^{29}Si nuclei

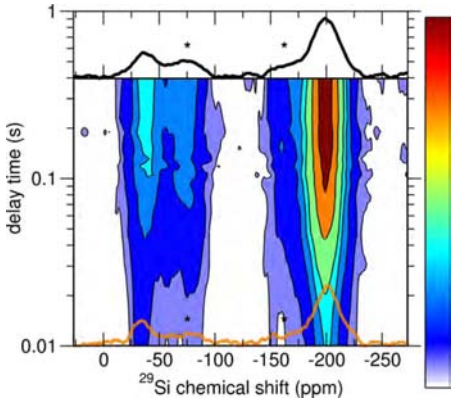

Figure 8. Solid-state ^{29}Si MAS NMR saturation−recovery spectra of $Ce_3Si_6N_{11}$ acquired at 295 K, 20 kHz MAS, and 18.8 T. Asterisks denote spinning sidebands. The traces at the top and bottom represent spectra from the longest and shortest delay times, respectively.

dx.doi.org/10.1021/ic402318k | Inorg. Chem. 2013, 52, 13730−13741

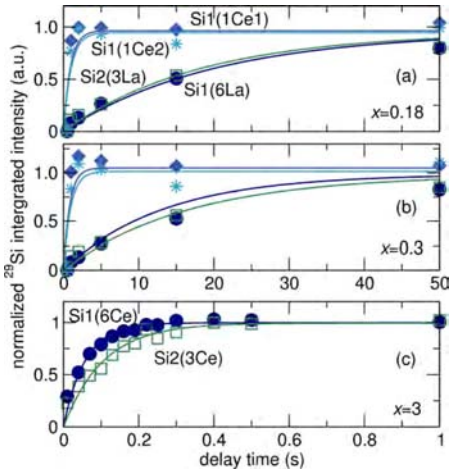

Figure 9. Integrated intensities from the saturation–recovery experiments for $La_{3-x}Ce_xSi_6N_{11}$ with x as indicated in (a) x = 0.18, (b) x = 0.3, and (c) x = 3. The signals from ^{29}Si nuclei near Ce^{3+} saturate much faster, indicating a dipolar interaction of the ^{29}Si nuclei with nearby Ce^{3+} ions.

(approximately −49 ppm and −61 ppm) saturate much slower than the other peaks. The bulk ^{29}Si peaks correspondingly have long relaxation times (~20 s) compared to the other peaks, which have relaxation times of ~1 s. This further supports that the peaks near −85 ppm and −100 ppm are from ^{29}Si nuclei near Ce^{3+}.

Local Structure of Ce^{3+} from Electron Spin Resonance (ESR). The site occupancy of Ce in $La_{3-x}Ce_xSi_6N_{11}$ can also be explored through electron spin resonance (ESR), along with other structural details. The ESR spectra of the solid-solution series in Figure 10 shows that the sharp peaks in low Ce

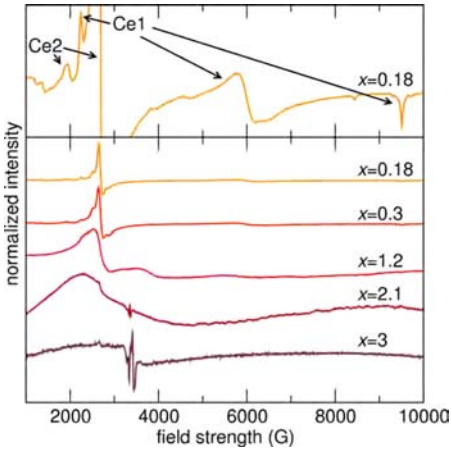

Figure 10. Electron spin resonance (ESR) of $La_{3-x}Ce_xSi_6N_{11}$ with x, as indicated. The top plot shows an expanded view of the $La_{2.82}Ce_{0.18}Si_6N_{11}$ material, showing the g_y and g_z tensor components of Ce(1). The feature near 3400 G for the x = 2.1 and x = 3 materials is an impurity. The spectra have been offset for clarity.

content samples broaden to nearly flat with increasing Ce content. This is due to Ce–Ce dipolar coupling, which decreases the unpaired electron relaxation time. Each site in the $La_3Si_6N_{11}$ structure has a different symmetry; the La(1)/Ce(1) site has C_s symmetry (one mirror plane), and the La(2)/Ce(2) site has C_4 symmetry (4-fold rotational symmetry). From this, it is expected that La site 2 would exhibit a higher-symmetry pattern than La site 1. The different peaks in the low-Ce content samples have been assigned to the two Ce sites, as indicated in Figure 10, based on this assumption. The Ce(2) site has a much larger peak area, indicating there is a preference for Ce to substitute on this site, consistent with the NMR and Rietveld results. Other small satellite peaks reside near the main Ce^{3+} features, and are satellite peaks from Ce^{3+} in slightly distorted lattice sites.

Evolution of Optical Properties. Since $La_{3-x}Ce_xSi_6N_{11}$ has been found to be an efficient yellow-emitting phosphor under 450-nm excitation,[37,71] we have investigated the spectroscopic properties of the various samples. The room-temperature excitation spectra in Figure 11b exhibit two strong

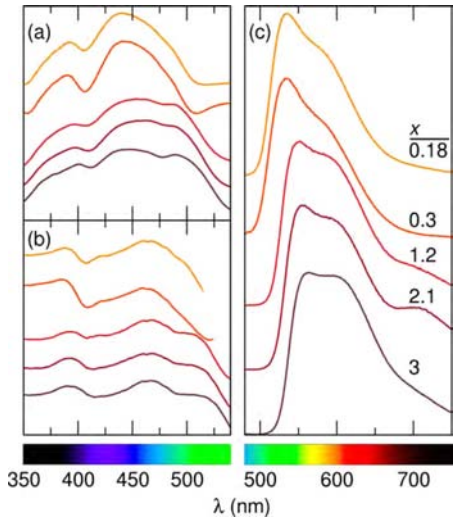

Figure 11. Room-temperature (a) Kubelka–Munk absorption, (b) excitation spectra collected with the emission wavelength of maximum intensity, and (c) emission spectra collected with the excitation wavelength of maximum intensity of $La_{3-x}Ce_xSi_6N_{11}$ materials, with the compositions x as indicated. The spectra have been offset for clarity.

and broad bands, located at 460 and 395 nm with shoulders peaking at ~500 nm and ~345 nm, corresponding to the transitions from the ground state ($^2F_{5/2}$) of the Ce^{3+} ion to the lowest lying d-states. As the splitting of the ground state due to the spin orbit coupling (2000 cm^{-1}) is much larger than the thermal energy k_BT at room temperature, absorption from the $^2F_{7/2}$ state can be neglected. A comparison of the excitation and absorption properties (obtained from diffuse reflectance measurements) shows that the same features can be found in both types of spectra, as shown in Figures 11a and 11b. Only a slight shift in the absolute positions of the bands is observed, if compared to the absorption data, which is mostly due to concentration and scattering effects,[72] since the absorption spectra have been collected from a sample diluted with $BaSO_4$. Regardless of Ce^{3+} concentration, the band gap of the unsubstituted $La_3Si_6N_{11}$ host is much larger than the phosphor's optical transitions. The calculated (HSE06) band gap is slightly larger than 4 eV, corresponding to 310 nm. Thus, excitations across the band gap of bands of $La_3Si_6N_{11}$ should not affect the optical properties in the visible region.

With increasing cerium concentration, x in $La_{3-x}Ce_xSi_6N_{11}$, a red shift of the position of the emission maximum is observed in the samples, as shown in Figure 11c and Table 3. This can be explained in terms of the strength of the crystal field splitting

dx.doi.org/10.1021/ic402318k | Inorg. Chem. 2013, 52, 13730–13741

Table 3. Spectroscopic Properties of the Various $La_{3-x}Ce_xSi_6N_{11}$ Materials

composition (x)	λ_{ex} (cm^{-1})	λ_{em} (cm^{-1})	ΔS (cm^{-1})
0.18	20120	17161, 19058	2959
0.30	20080	17116, 19015	2964
1.20	19801	16809, 18695	2992
2.10	19531	16552, 18461	2979
3.00	19342	16368, 18246	2974

(Dq or Δ), which Dorenbos has shown to be related to the Ce-anion distance by an R^{-2} relationship.[73] We find that, with increasing cerium concentration, the Ce^{3+}–N bond lengths decrease, leading to an increase in the crystal field splitting. The variance of the (La/Ce)–N bonds also increases with increasing x; from $x = 0.18$ to $x = 1.2$, the standard deviation of La(1)/Ce(1)–N bond lengths increases by 5%, and by 21% for La(2)/Ce(2)–N bond lengths. This increase in distortion of the bond length distribution could also contribute to an increase in crystal field splitting. A larger Dq (or Δ) thus means that the energy difference between the ground state(s) of cerium and the lowest d-state is reduced, shifting the emission maximum into the lower energy (i.e., red) part of the visible spectrum. More evidence for this increase in crystal field splitting strength can be found in the excitation/absorption spectra; with increasing cerium content (i.e., decreasing bond length), there is a significant shift toward lower energies in the position of the lowest energy excitation/absorption band, which can be seen in Figures 11a and 11b.

The low-temperature (77 K) emission spectra in Figure 12b show the same shift toward lower energies with increasing

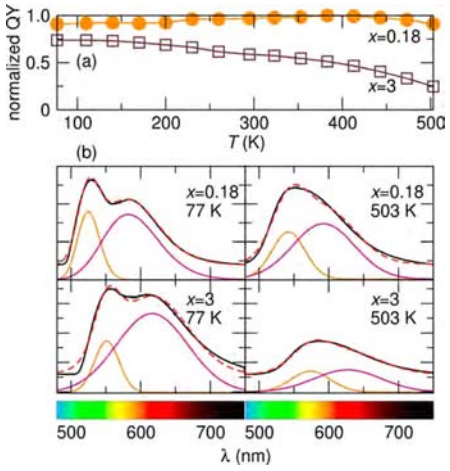

Figure 12. (a) Temperature-dependent normalized quantum yield for the $x = 0.18$ and $x = 3$ $La_{3-x}Ce_xSi_6N_{11}$ materials, and (b) emission spectra of the $x = 0.18$ and $x = 3$ materials at 77 and 503 K with the fits to the data shown.

cerium concentration as those observed at room temperature. The splitting of the emission band, partially observed at room temperature, becomes more pronounced at lower temperatures, and two very distinct bands are observed. These two bands arise from the transitions of the lowest lying 5d-state to the $^2F_{5/2}$ and $^2F_{7/2}$ states of the Ce ion. To further analyze these transitions, peak deconvolution for all cerium concentrations has been carried out. Although four Gaussian peaks can be used to fit the data, the data are represented well with only two Gaussians, suggesting emission from both sites is very similar. This is not surprising, since both Ce sites are eight-coordinated and have bond distances that only differ by ~2%. Other systems with two Ce sites that have similar coordination numbers, such as previously observed in lanthanum silicon oxynitride phosphors[74] and $Sr_{2.975}Ce_{0.025}Al_{1-x}Si_xO_{4+x}F_{1-x}$,[11] also display an emission that can be fit well with two Gaussian curves. The fits yield two bands that are separated by ~1900 cm^{-1} in all samples, which is a measure of the magnitude of the spin–orbit coupling of the 4f levels. This result is consistent with the values of ~2000 cm^{-1} typically found for Ce^{3+} in the literature.[75] The peak deconvolution also shows that with increasing cerium concentration, the emission band at higher energies decreased in intensity compared to the low-energy band. The ratio of these two bands drops from 0.35 ($x = 0.18$) to ~0.23 ($x = 3.00$). This effect has been explained with more efficient reabsorption at higher cerium concentrations.[30] In addition, Dorenbos has shown that the Stokes shift, determined as the difference between the excitation band with the lowest energy and emission with the highest energy, can be considered as a feature of the host once a trivalent lanthanide ion (Ln^{3+}) is introduced into a host lattice.[76] When taking the shoulder at ~495–520 nm as the excitation band with the lowest energy, we find values of ~2975 cm^{-1} for all samples (see Table 3).

To investigate the thermal robustness of the materials, temperature-dependent emission spectra have been recorded. The right column in Figure 12b displays the emission spectra (under 450 nm excitation) at a temperature of 503 K. It can clearly be seen that, in the $x = 0.18$ material, there is almost no sign of temperature quenching (also see Table 4). Materials

Table 4. Temperature-Dependent Spectroscopic Properties (Normalized Quantum Yield and Quenching Temperature) of the Various $La_{3-x}Ce_xSi_6N_{11}$ Materials

composition (x)	$QY_{77\ K}$ (%)	$QY_{298\ K}$ (%)	$QY_{503\ K}$ (%)	$T_{1/2}$ (K)
0.18	0.94	1.00	0.95	>503
0.30	0.96	0.98	0.86	>503
1.20	0.65	0.63	0.38	>503
2.10	0.71	0.62	0.30	480
3.00	0.77	0.61	0.25	450

with $x \leq 0.3$ show high emission intensities and a high quantum yield over the complete measured temperature range. If $x \geq 1.2$, the quenching effects become more pronounced, which is also evident in the quenching temperature $T_{1/2}$ that has been calculated for the different compounds. $T_{1/2}$ is usually defined as the temperature at which the emission intensity has dropped to 50% of the value obtained at low temperatures (4.2 or 77 K). As can be seen in Table 4, for samples with x up to 1.2, we have not observed temperature quenching in the measured temperature range. For the samples with $x = 2.1$ and 3.0, $T_{1/2}$ has been found to be 480 and 450 K, respectively. Even with full Ce substitution, a strong emission is still present. The $Ce_3Si_6N_{11}$ material exhibits a quantum yield of ~1/4 of that of the $La_{2.82}Ce_{0.18}Si_6N_{11}$ material at 503 K, which is remarkable for a stoichiometric cerium compound.

One very interesting feature of the $La_{3-x}Ce_xSi_6N_{11}$ family of phosphors is the absence of complete concentration quenching at higher cerium concentrations. Usually, once a certain critical concentration is exceeded, nonradiative energy transfer mechanisms become more efficient (due to the increased probability of two emission centers being proximal) and the excitation energy is transferred between the activator ions until

dx.doi.org/10.1021/ic402318k | Inorg. Chem. 2013, 52, 13730–13741

it has reached some type of trap, such as defects or surface states. However, some cerium compounds, such as CeF_3[30] and $CeMgAl_{11}O_{19}$[31] maintain emission even with 100% Ce substitution on the RE site. The lack of concentration quenching in these compounds has been attributed to large Stokes shifts, and possibly to inefficient $Ce^{3+}-Ce^{3+}$ dipole transfer. These reasons also perhaps contribute to why complete concentration quenching is not observed in $La_{3-x}Ce_xSi_6N_{11}$. In addition, Ce does not distort the $La_{3-x}Ce_xSi_6N_{11}$ lattice, since 8-coordinate Ce^{3+} and La have nearly the same values of ionic radii (1.143 Å and 1.16 Å, respectively).[63] This would mean distorted Ce^{3+} sites, which would act as a trap for excited Ce^{3+} electrons, should be almost nonexistent. Finally, the short decay times, as presented below may play a role in avoiding strong concentration quenching. These short decay times decrease the time available—and, hence, probability—for nonradiative transitions to occur. Similarly, in CeF_3, a short 20 ns decay time has been found.[77]

Blasse has proposed a model[78] that allows one to estimate the so-called "critical distance" (R_C) of energy transfer, which has been described as the distance for which the transfer probability equals the emission probability of the emitting ion, from the concentration quenching. R_C can be calculated using the relation

$$R_C \approx 2\left(\frac{3V}{4\pi x_C N}\right)^{1/3} \quad (2)$$

where V is the volume of the unit cell, x_C the critical quenching concentration, and N is the sum of Wyckoff multiplicities for the potential substitution sites in the unit cell. Using the volume value obtained from the Rietveld refinement (V = 502.8 Å^3), and x_C = 0.06 (the concentration for which the highest emission intensity was observed) and N = 6, we find a critical distance for energy transfer of ~13.9 Å. Since the luminescence even in the stoichiometric cerium compound $Ce_3Si_6N_{11}$ is not quenched completely, we can use a volume of V = 497.6 Å^3 from the Rietveld refinement, and x_C = 1, which leads to a value of 5.4 Å. Typical Ce−Ce distances within the host lattice are 3.7 Å for Ce(1)−Ce(1) and Ce(1)−Ce(2) distances, and 4.8 Å for Ce(2)−Ce(2) pairs. Usually, the critical radius is much larger than typical next-nearest neighbor distances. However, if they are of the same order of magnitude, concentration quenching might be absent or very weak, as we find in the case of $Ce_3Si_6N_{11}$; thus, even this compound with full Ce substitution for La does not show complete quenching of the luminescence.

Another way of determining the concentration quenching effect is through the investigation of the concentration dependence of the luminescence lifetime; therefore, the time-resolved luminescence properties are displayed in Figure 13. The samples have been excited with 440 nm light and the emission between 530 nm and 560 nm was monitored. For all samples, decay times of ~40 ns are found, with a single exponential fit describing the data well. The single exponential fit suggests both Ce sites emit with a similar decay time. A similar result was found in an oxyfluoride phosphor with two separate Ce sites,[11] and is much shorter than the 60−65 ns decay time found for YAG:Ce^{3+}.[79] Only a very slight decrease is observed with increasing cerium concentration (from 42 ns in the sample with x = 0.18 to ~37 ns in $Ce_3Si_6N_{11}$). The obtained values are very comparable to typically observed decay

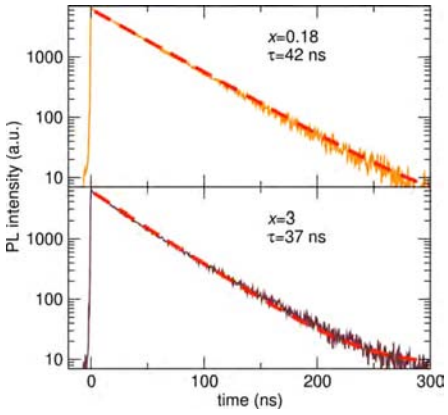

Figure 13. Photoluminescence decay curves for the various $La_{3-x}Ce_xSi_6N_{11}$ samples with different cerium concentrations under 440-nm pulsed-laser excitation.

times for 5d−4f transitions in Ce^{3+} and match the observations of Suehiro et al.[71] for $(La,Ca)_3Si_6N_{11}$:Ce^{3+} very well.

CONCLUSIONS

Structural characterization of $La_{3-x}Ce_xSi_6N_{11}$ using a combination of scattering studies and magnetic resonance has shown Ce prefers to substitute on one of the two La sites in a manner that better satisfies its bond valence. Rietveld refinements of synchrotron X-ray and neutron scattering data show $La_{3-x}Ce_xSi_6N_{11}$ to have a very rigid crystal structure, with small U_{iso} values corresponding to high Debye temperatures, which is potentially a reason for the strong thermal robustness of luminescence observed in these compounds. The high Debye temperature of the host lattice is corroborated from ab initio calculations. Optical excitation and emission spectra suggest that both Ce sites emit at very similar energies with decay times of ~40 ns. The time decay of $La_{3-x}Ce_xSi_6N_{11}$ decreases only slightly, from x = 0.18 to x = 3. The absence of complete concentration quenching in $Ce_3Si_6N_{11}$ is likely due to the large Stokes shift, inefficient $Ce^{3+}-Ce^{3+}$ dipolar transfer, the fact that Ce does not distort the lattice, and the short decay times of ~40 ns. These insights into this important phosphor material suggest guidelines for the development of new materials.

ASSOCIATED CONTENT

Supporting Information

Additional optical measurement experimental details and discussion, data from Rietveld refinements, and NMR data. This material is available free of charge via the Internet at http://pubs.acs.org/.

AUTHOR INFORMATION

Corresponding Author

*Tel.: (805) 893-6129. Fax: (805) 893-8797. E-mail: seshadri@mrl.ucsb.edu.

Notes

The authors declare no competing financial interest.

ACKNOWLEDGMENTS

N.C.G. has been supported by the ConvEne IGERT Program (NSF-DGE No. 0801627). The research carried out here made extensive use of shared experimental facilities of the Materials Research Laboratory: The MRL Central Facilities are

supported by the MRSEC Program of the NSF under Award No. DMR 1121053; a member of the NSF-funded Materials Research Facilities Network (www.mrfn.org). Use of the Advanced Photon Source at Argonne National Laboratory was supported by the U.S. Department of Energy, Office of Science, Office of Basic Energy Sciences (under Contract No. DE-AC02-06CH11357). The authors thank Joan Siewenie for assistance with data collection at NPDF. This work has benefited from the use of NPDF and HIPD at the Lujan Center, funded by DOE Office of Basic Energy Sciences; LANL is operated by Los Alamos National Security LLC (under No. DE-AC52-06NA25396).

REFERENCES

(1) Schubert, E. F.; Kim, J. K. *Science* **2005**, *308*, 1274−1278.
(2) Nakamura, S. *Mater. Res. Bull.* **2009**, *34*, 101−107.
(3) Pimputkar, S.; Speck, J. S.; Denbaars, S. P.; Nakamura, S. *Nat. Photonics* **2009**, *3*, 2−4.
(4) George, N. C.; Denault, K. A.; Seshadri, R. *Ann. Rev. Mater. Res.* **2013**, *43*, 2:1−2:21.
(5) Shur, M. S.; Zukauskas, R. *Proc. IEEE* **2005**, *93*, 1691−1703.
(6) Krames, M. R.; Shchekin, O. B.; Müller-Mach, R.; Müller, G. O.; Zhou, L.; Harbers, G.; Craford, M. G. *J. Disp. Technol.* **2007**, *3*, 160−175.
(7) Bando, K.; Sakano, K.; Noguchi, Y.; Shimizu, Y. *J. Light Visual Environ.* **1998**, *22*, 2−5.
(8) Ye, S.; Xiao, F.; Pan, Y.; Ma, Y.; Zhang, Q. *Mater. Sci. Eng., R.* **2010**, *71*, 1−34.
(9) Wu, Y.-C.; Wang, D.-Y.; Chen, T.-M.; Lee, C.-S.; Chen, K.-J.; Kuo, H.-c. *ACS Appl. Mater. Interfaces* **2011**, *3*, 3195−3199.
(10) Xia, Z.; Wang, X.; Wang, Y.; Liao, L.; Jing, X. *Inorg. Chem.* **2011**, *50*, 10134−10142.
(11) Im, W. B.; George, N.; Kurzman, J.; Brinkley, S.; Mikhailovsky, A.; Hu, J.; Chmelka, B. F.; DenBaars, S. P.; Seshadri, R. *Adv. Mater.* **2011**, *23*, 2300−2305.
(12) Shang, M.; Li, G.; Kang, X.; Yang, D.; Geng, D.; Lin, J. *ACS Appl. Mater. Interfaces* **2011**, *3*, 2738−2746.
(13) Wang, X.-M.; Wang, C.-H.; Kuang, X.-J.; Zou, R.-Q.; Wang, Y.-X.; Jing, X.-P. *Inorg. Chem.* **2012**, *51*, 3540−3547.
(14) Mueller-Mach, R.; Mueller, G.; Krames, M. R.; Höppe, H. A.; Stadler, F.; Schnick, W.; Juestel, T.; Schmidt, P. *Phys. Status Solidi A* **2005**, *202*, 1727−1732.
(15) Xie, R.; Hirosaki, N. *Sci. Technol. Adv. Mater.* **2007**, *8*, 588−600.
(16) Zeuner, M.; Pagano, S.; Matthes, P.; Bichler, D.; Johrendt, D.; Harmening, T.; Pöttgen, R.; Schnick, W. *J. Am. Chem. Soc.* **2009**, *131*, 11242−11248.
(17) Zeuner, M.; Pagano, S.; Schnick, W. *Angew. Chem., Int. Ed.* **2011**, *50*, 7754−7775.
(18) Li, Y.; van Steen, J.; van Krevel, J.; Botty, G.; Delsing, A.; DiSalvo, F.; de With, G.; Hintzen, H. *J. Alloys Compd.* **2006**, *417*, 273−279.
(19) Brgoch, J.; DenBaars, S. P.; Seshadri, R. *J. Phys. Chem. C* **2013**, *117*, 17955−17959.
(20) van Krevel, J.; van Rutten, J.; Mandal, H.; Hintzen, H.; Metselaar, R. *J. Solid State Chem.* **2002**, *165*, 19−24.
(21) Dorenbos, P. *J. Phys.: Condens. Matter* **2003**, *15*, 4797−4807.
(22) Mikami, M.; Kijima, N. *Opt. Mater.* **2010**, *33*, 145−148.
(23) Mikami, M.; Kijima, N.; Bertrand, B.; Stankovski, M.; Gonze, X. *IOP Conf. Ser.: Mater. Sci. Eng.* **2011**, *18*, 102001.
(24) van Krevel, J.; Hintzen, H.; Metselaar, R.; Meijerink, A. *J. Alloys Compd.* **1998**, *268*, 272−277.
(25) Kurushima, T.; Gundiah, G.; Shimomura, Y.; Mikami, M.; Kijima, N.; Cheetham, A. K. *J. Electrochem. Soc.* **2010**, *157*, J64−J68.
(26) Uheda, K.; Hirosaki, N.; Yamamoto, H. *Phys. Status Solidi A* **2006**, *203*, 2712−2717.
(27) Duan, C. J.; Wang, X. J.; Otten, W. M.; Delsing, A. C. A.; Zhao, J. T.; Hintzen, H. T. *Chem. Mater.* **2008**, *20*, 1597−1605.
(28) Li, Y. Q.; Hirosaki, N.; Xie, R. J.; Takeda, T.; Mitomo, M. *Chem. Mater.* **2008**, *20*, 6704−6714.
(29) Suehiro, T.; Hirosaki, N.; Xie, R.; Sato, T. *Appl. Phys. Lett.* **2009**, *95*, 051903-1−051903-3.
(30) Blasse, G.; Bril, A. *Chem. Phys.* **1969**, *51*, 3252−3254.
(31) Verstegen, J.; Sommerdijk, J.; Verriet, J. *J. Lumin.* **1973**, *6*, 425−431.
(32) Danielson, E.; Devenney, M.; Giaquinta, D. M.; Golden, J. H.; Haushalter, R. C.; McFarland, E. W.; Poojary, D. M.; Reaves, C. M.; Weinberg, W.; Wu, X. D. *J. Mol. Struct.* **1998**, *470*, 229−235.
(33) Pieterson, L. v.; Soverna, S.; Meijerink, A. *J. Electrochem. Soc.* **2000**, *147*, 4688−4691.
(34) Gaude, J.; Lang, J.; Louer, D. *Rev. Chem. Miner.* **1983**, *20*, 523−527.
(35) Woike, M.; Jeitschko, W. *Inorg. Chem.* **1995**, *34*, 5105−5108.
(36) Schlieper, T.; Schnick, W. *Z. Anorg. Allg. Chem.* **1995**, *621*, 1535−1538.
(37) Kijima, N.; Seto, T.; Hirosaki, N. *ECS Trans.* **2009**, *25*, 247−252.
(38) Seto, T.; Kijima, N. *Phosphor and production method thereof*, U.S. Patent Publication No. US 2010/0085728 A1 U.S. Classification: 362/84, 2009.
(39) Kresse, G.; Furthmuller, J. *Phys. Rev. B* **1993**, *47*, 558−561.
(40) Kresse, G.; Furthmuller, J. *Phys. Rev. B* **1996**, *54*, 11169−11186.
(41) Blöchl, P. *Phys. Rev. B* **1994**, *50*, 17953−17979.
(42) Kresse, G.; Joubert, D. *Phys. Rev. B* **1999**, *59*, 1758−1775.
(43) Le Page, Y.; Saxe, P. *Phys. Rev. B* **2002**, *65*, 104104.
(44) Perdew, J.; Burke, K.; Ernzerhof, M. *Phys. Rev. Lett.* **1996**, *77*, 3865−3868.
(45) Monkhorst, H. J.; Pack, J. D. *Phys. Rev. B* **1976**, *13*, 5188.
(46) Heyd, J.; Scuseria, G. E.; Ernzerhof, M. *J. Chem. Phys.* **2003**, *118*, 8207−8215.
(47) Heyd, J.; Scuseria, G. E.; Ernzerhof, M. *J. Chem. Phys.* **2006**, *124*, 219906.
(48) Wang, J.; Toby, B. H.; Lee, P. L.; Ribaud, L.; Antao, S. M.; Kurtz, C.; Ramanathan, M.; Von Dreele, R. B.; Beno, M. A. *Rev. Sci. Instrum.* **2008**, *79*, 085105-1−085105-7.
(49) Dalesio, L. R.; Hill, J. O.; Kraimer, M.; Lewis, S.; Murray, D.; Hunt, S.; Watson, W.; Clausen, M.; Dalesio, J. *Nucl. Instrum. Methods A* **1994**, *352*, 179−184.
(50) Lee, P. L.; Shu, D.; Ramanathan, M.; Preissner, C.; Wang, J.; Beno, M. A.; Von Dreele, R. B.; Ribaud, L.; Kurtz, C.; Antao, S. M.; Jiao, X.; Toby, B. H. *J. Synchrotron Radiat.* **2008**, *15*, 427−432.
(51) Toby, B. H. *J. Appl. Crystallogr.* **2001**, *34*, 210−213.
(52) Larson, A. C.; Dreele, R. B. V. *Technical Report No. LAUR 86-748*, Los Alamos National Laboratory, Albuquerque, NM, 2000.
(53) Le Bail, A.; Duroy, H.; Fourquet, J. *Mater. Res. Bull.* **1988**, *23*, 447−452.
(54) Momma, K.; Izumi, F. *J. Appl. Crystallogr.* **2011**, *44*, 1272−1276.
(55) Willis, B. T. M.; Pryor, A. W. *Thermal Vibrations in Crystallography*; Cambridge University Press: Oxford, U.K., 1975.
(56) Massiot, D.; Fayon, F.; Capron, M.; King, I.; Le Calvé, S.; Alonso, B.; Durand, J.-O.; Bujoli, B.; Gan, Z.; Hoatson, G. *Magn. Reson. Chem.* **2002**, *40*, 70−76.
(57) Greenham, N. C.; Samuel, I. D. W.; Hayes, G. R.; Phillips, R. T.; Kessener, Y. A. R. R.; Moratti, S. C.; Holmes, A. B.; Friend, R. H. *Chem. Phys. Lett.* **1995**, *241*, 89−96.
(58) Birkel, A.; Denault, K. A.; George, N. C.; Doll, C. E.; Héry, B.; Mikhailovsky, A. A.; Birkel, C. S.; Hong, B.-C.; Seshadri, R. *Chem. Mater.* **2012**, *24*, 1198−1204.
(59) Im, W. B.; Brinkley, S.; Hu, J.; Mikhailovsky, A.; DenBaars, S. P.; Seshadri, R. *Chem. Mater.* **2010**, *22*, 2842−2849.
(60) Kubelka, P.; Munk, F. *Z. Tech. Phys.* **1931**, 593−601.
(61) Becker, W. *Advanced Time-Correlated Single Photon Counting Techniques*; Springer: Berlin, Heidelberg, New York, 2005; Vol. *81*.
(62) Shimomura, Y.; Kurushima, T.; Kijima, N. *J. Electrochem. Soc.* **2007**, *154*, J234.
(63) Shannon, R. D. *Acta Crystallogr., Sect. A: Cryst. Phys., Diffr., Theor. Gen. Crystallogr.* **1976**, *32*, 751−767.

(64) Trzesowska, A.; Kruszynski, R.; Bartczak, T. J. *Acta Crystallogr., Sect. B: Struct. Sci.* **2005**, *61*, 429−434.
(65) Grey, C. P.; Smith, M. E.; Cheetham, A. K.; Dobson, C. M.; Dupree, R. *J. Am. Chem. Soc.* **1990**, *112*, 4670−4675.
(66) Grey, C. P.; Dobson, C. M.; Cheetham, A. K.; Jakeman, R. J. B. *J. Am. Chem. Soc.* **1989**, *111*, 505−511.
(67) Harazono, T.; Yokota, E.; Uchida, H.; Watanabe, T. *Bull. Chem. Soc. Jpn.* **1998**, *71*, 2797−2805.
(68) George, N. C.; Pell, A. J.; Dantelle, G.; Page, K.; Llobet, A.; Balasubramanian, M.; Pintacuda, G.; Chmelka, B. F.; Seshadri, R. *Chem. Mater.* **2013**, *25*, 3979−3995.
(69) Abragam, A. *Principles of Nuclear Magnetism*; Clarendon Press: Oxford, U.K., 1961.
(70) Bleaney, B. *J. Magn. Reson.* **1972**, *8*, 91−100.
(71) Suehiro, T.; Hirosaki, N.; Xie, R.-J. *ACS Appl. Mater. Interfaces* **2011**, *3*, 811−816.
(72) Im, W. B.; Page, K.; DenBaars, S. P.; Seshadri, R. *J. Mater. Chem.* **2009**, *19*, 8761−8766.
(73) Dorenbos, P. *Phys. Rev. B* **2001**, *64*, 125117.
(74) Dierre, B.; Xie, R.-J.; Hirosaki, N.; Sekiguchi, T. *J. Mater. Res.* **2011**, *22*, 1933−1941.
(75) Blasse, G.; Bril, A. *Appl. Phys. Lett.* **1967**, *11*, 53.
(76) Dorenbos, P. *J. Lumin.* **2000**, *91*, 155−176.
(77) Moses, W.; Derenzo, S. *IEEE Trans. Nucl. Sci.* **1989**, *36*, 173−176.
(78) Blasse, G. P. R. L. *Phys. Lett.* **1968**, *28A*, 444−445.
(79) Bachmann, V.; Ronda, C.; Meijerink, A. *Chem. Mater.* **2009**, *21*, 2077−2084.